Finite-temperature valence-bond-solid transitions and thermodynamic properties of interacting SU(2N) Dirac fermions

Zhichao Zhou,[1] Da Wang,[2] Congjun Wu,[3] and Yu Wang[1,*]

[1]*School of Physics and Technology, Wuhan University, Wuhan 430072, China*

[2]*National Laboratory of Solid State Microstructures and School of Physics, Nanjing University, Nanjing, 210093, China*

[3]*Department of Physics, University of California, San Diego, California 92093, USA*

(Received 22 August 2016; revised manuscript received 2 January 2017; published 21 February 2017)

We investigate the SU(2N) symmetry effects with $2N > 2$ on the two-dimensional interacting Dirac fermions at finite temperatures, including the valence-bond-solid transition, the Pomeranchuk effect, the compressibility, and the uniform spin susceptibility, by performing the determinant quantum Monte Carlo simulations of the half-filled SU(2N) Hubbard model on a honeycomb lattice. The columnar valence-bond-solid (cVBS) phase only breaks the threefold discrete symmetry and thus can survive at finite temperatures. The disordered phase in the weak coupling regime is the thermal Dirac semi-metal state, while in the strong coupling regime it is largely a Mott state in which the cVBS order is thermally melted. The calculated entropy-temperature relations for various values of the Hubbard interaction U show that the Pomeranchuk effect occurs when the specific entropy is below a characteristic value of S^*—the maximal entropy per particle from the spin channel of local moments. The SU(2N) symmetry enhances the Pomeranchuk effect, which facilitates the interaction-induced adiabatic cooling. Our work sheds light on future explorations of novel states of matter with ultracold large-spin alkaline fermions.

DOI: 10.1103/PhysRevB.95.085128

I. INTRODUCTION

The low-energy quasiparticles on a honeycomb lattice exhibit the two-dimensional (2D) massless Dirac-fermion-type band structure. The interplay between charge and spin degrees of freedom together with the Dirac band structure brings novel features of quantum phases, which has become a major research focus in condensed matter physics since the discovery of graphene [1]. The strong interaction effects in 2D Dirac fermion systems have been investigated extensively by applying quantum Monte Carlo (QMC) simulations to the SU(2) Hubbard model, a paradigmatic model for Mott physics of interacting electrons [2,3]. Because of the bipartite nature of the honeycomb lattice, it exhibits the antiferromagnetic (AF) long-range order in the Mott-insulating phase. The transition from the Dirac semimetal phase to the AF insulating phase is found to be continuous [4–6].

Dirac fermions are not unique to high energy and solid state systems and also can be realized in optical lattices loaded with ultracold fermionic atoms. Unlike spin-$\frac{1}{2}$ electrons in solids which usually possess the SU(2) symmetry, ultracold fermions often carry large hyperfine spins. As proposed earlier by one of the authors, Hu and Zhang [7], ultracold alkali and alkaline-earth fermions provide an opportunity to study high symmetries that are typically studied in the high energy context. For example, the simplest large-spin fermions of spin-$\frac{3}{2}$ in optical lattices generically possess the high symmetry of Sp(4), or, isomorphically SO(5), without fine tuning [7]. If the interaction is spin independent, the symmetry is enlarged to SU(4). These high symmetries are expected to give rise to exotic quantum phases difficult to access in solids, which provide important guidance in analyzing novel many-body physics with multicomponent fermions [8]. On the other hand, it has been pointed out that the alkaline-earth fermion systems respect the SU(2N) symmetry, owing to their closed shell electron structure. Their hyperfine spins are simply nuclear spins, and thus the interatomic scatterings are spin independent, leading to the SU(2N) symmetry [9,10]. Excitingly, the recent rapid progress of ultracold atom experiments have already realized these SU(2N) symmetric systems [11–15]. The quantum degenerate temperatures have been reached in alkaline-earth atoms with the large hyperfine spins, e.g., ^{173}Yb with SU(6) symmetry [11] and ^{87}Sr with the SU(10) symmetry [12]. Excitingly, an SU(6) Mott insulator has also been realized with ^{173}Yb atoms in the optical lattice, and the Mott insulating gap has been observed in the shaking lattice experiment [13].

It will be interesting to combine the SU(2N) symmetry and the 2D Dirac fermion together, which can be realized by loading large spin alkaline-earth fermions into the honeycomb optical lattice, to investigate novel physics absent in the SU(2) Hubbard model of Dirac fermions. In a recent paper [16], we investigated the novel effects of the SU(2N) symmetries on quantum many-body physics of Dirac fermions, including quantum magnetism and the Dirac semimetal-to-Mott insulator transitions, by performing the projector determinant quantum Monte Carlo simulations of the half-filled SU(2N) Hubbard model on a honeycomb lattice. We found that, fundamentally different from the usual SU(2) Mott-insulating phase which exhibits the AF Néel ordering, the SU(4) and SU(6) Mott-insulating phases are identified with the valence-bond-solid (VBS) order. Both the columnar VBS (cVBS) and the plaquette VBS (pVBS) break the same type of symmetry and compete, and the ground states are found to exhibit the cVBS order. The nature of the Dirac semimetal-to-cVBS order transition has been analyzed at the mean-field level. It unveils the possibility of an exotic second order quantum phase transition seemingly forbidden by the Ginzburg-Landau theory, which is also investigated and confirmed by the renormalization group analysis [17–20]. Besides, our mean-field analysis also points out that the semimetal-to-cVBS transition at finite temperatures is still the first order.

*yu.wang@whu.edu.cn

In this work, we investigate the thermodynamic properties of the 2D SU($2N$) Hubbard model on the honeycomb lattice by employing the unbiased nonperturbative determinant QMC simulations. We focus on the thermal cVBS transition and the interaction-induced Pomeranchuk effect of the SU($2N$) Dirac fermions. Since the cVBS state only breaks the discrete symmetry of lattice translation, it can survive at finite temperatures and the transition to the disordered state can take place at finite temperatures. The weak coupling Dirac-semimetal regime and the strong coupling disordered Mott-insulating state are connected at finite temperatures. The finite-temperature simulation studies of Hubbard models show that the Pomeranchuk effect occurs when the specific entropy is below a characteristic value of S^*, where S^* represents the maximum amount of specific entropy carried by the spin channel. The Pomeranchuk effect is dependent on the symmetry and the lattice structure. We have shown that the multicomponent SU($2N$) Hubbard model on a honeycomb lattice significantly facilitates the Pomeranchuk effect, which starts with even relatively high entropies. Other thermodynamic properties, including the onsite particle number fluctuations, compressibility, and the uniform spin susceptibility, are also analyzed.

The rest of the paper is organized as follows. In Sec. II, the model Hamiltonian and parameters for determinant QMC (DQMC) are introduced. In Sec. III, the thermal VBS transition is studied. The entropy and the on-site occupation number are studied in Sec. IV. Subsequently in Sec. V, the density compressibility and uniform spin susceptibilities are investigated. The conclusions are drawn in Sec. VI.

II. MODEL AND METHOD

A. The SU($2N$) Hubbard model

At half-filling, the Hubbard model with SU($2N$) symmetry takes the following form on a honeycomb lattice,

$$H = -t \sum_{i\in A,\hat{e}_j;\alpha} (c^\dagger_{i\alpha} c_{i+\hat{e}_j,\alpha} + \text{H.c.}) + \frac{U}{2} \sum_{i\in A\oplus B} (n_i - N)^2, \tag{1}$$

where A and B denote two sublattices of the honeycomb lattice; $\hat{e}_j$'s with $j = 1,2,3$ are vectors connecting each site with its three nearest neighbors; the spin index α runs from 1 to $2N$ and $n_i = \sum_\alpha c^\dagger_{i\alpha} c_{i\alpha}$ is the particle number operator on site i; t and U are the nearest-neighbor hopping integral and the on-site Coulomb repulsion, respectively. The chemical potential μ vanishes in the grand canonical Hamiltonian due to half-filling. U is defined in the following convention: In the atomic limit, $t/U \to 0$, if a single fermion is removed from one site and put on any other site on the half-filled 2D system, the energy cost of this charge excitation is U, which is independent of N.

B. The numerical method

We employ the DQMC method based on the Blankenbecler-Scalapino-Sugar algorithm [21]. QMC is a widely used nonperturbative and unbiased numerical method for studying 2D strongly correlated systems. Compared to other methods, the major advantage is that it is scalable to large sizes and capable of yielding asymptotically exact results provided that the sign problem is absent. The half-filled SU($2N$) Hubbard model is free of the sign problem in the bipartite lattices. In the DQMC simulations of the SU(4) and SU(6) Hubbard models with repulsive interactions, an exact Hubbard-Stratonovich (HS) decomposition is performed in the density channel involving complex numbers, which maintains the SU($2N$) symmetry during the HS decomposition [22]. The method of the HS decomposition is explained in Appendix B.

The parameters of the QMC simulations are presented below. Unless specifically stated, the time discretization parameter $\Delta\tau$ is set to $1/30$ at least, ensuring the convergence of the second-order Suzuki-Trotter decomposition. The $2 \times L \times L$ honeycomb lattice with $L = 9$ is simulated under the periodic boundary condition which preserves the translational symmetry. The finite-size effect on the entropy-temperature relations is analyzed in Appendix A. For a typical data point, we use 10 QMC bins each of which includes 2000 warmup steps and 8000 measurements. To investigate the thermal phase transition by the finite-size scaling, the $2 \times L \times L$ honeycomb lattices with $L = 6,9,12,15$ are simulated with at least 20 QMC bins, each bin containing 500 warmup steps and 500 measurements. In our simulations, the Hubbard U and temperature T are given in the unit of t.

C. The order parameters

We define three bonds attached to site i as

$$d_{i,\hat{e}_j} = \frac{1}{2N} \sum_{\alpha=1}^{2N} (c^\dagger_{i,\alpha} c_{i+\hat{e}_j,\alpha} + \text{H.c.}), \tag{2}$$

where $j = 1,2,3$ represent three different bond orientations. The cVBS and pVBS orders are defined in the same form as

$$D_K(L) = \frac{1}{L^2} \sum_{i\in A} \left(d_{i,\hat{e}_a} + \omega d_{i,\hat{e}_b} + \omega^2 d_{i,\hat{e}_c}\right) e^{i\vec{K}\cdot\vec{r}_i}, \tag{3}$$

where $\omega = e^{i\frac{2}{3}\pi}$ and $\vec{K} = (\frac{4\pi}{3\sqrt{3}a_0}, 0)$. Their configurations are depicted in Fig. 1. Following Ref. [16], the difference between cVBS and pVBS can be distinguished through the following parameter,

$$W = \int dz dz^* P(z,z^*) \cos 3\theta, \tag{4}$$

where $z = D_K$, $\theta = \arg(z)$, and $P(z,z^*)$ is the density of probability that appears in Monte Carlo samplings. For the

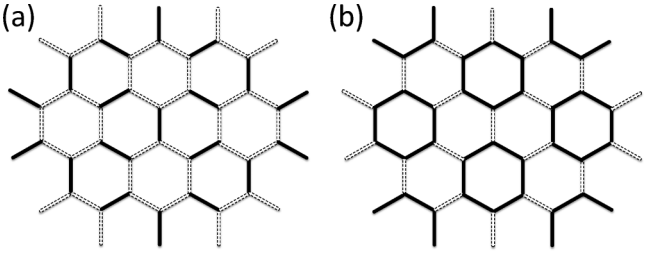

FIG. 1. The cVBS (a) and pVBS (b) configurations break the threefold discrete symmetry and exhibit a $\sqrt{3} \times \sqrt{3}$ superunit cell. (This figure is taken from Ref. [16].)

ideal cVBS and pVBS states without fluctuations, W equals 1 and -1, respectively. Certainly, fluctuations weaken the magnitudes of W, nevertheless, the sign of W can be used to distinguish whether the ordering is cVBS or pVBS. For the isotropic state, $W = 0$.

III. THE FINITE TEMPERATURE VBS TRANSITION

In Ref. [16], the Dirac semimetal-to-cVBS transitions are shown to occur in the ground states of SU(4) and SU(6) Hubbard models on a honeycomb lattice. Quantum spin fluctuations are enhanced with increasing $2N$, and thus the strength of cVBS order in the SU(6) case is stronger than that in the SU(4) case. In the SU(6) case, the cVBS order starts to appear around $U/t \approx 11$ and grows with increasing U until reaching the peak value around $U/t \approx 14$, and then decreases as U further increases. The cVBS state breaks the threefold discrete symmetry exhibiting the $\sqrt{3} \times \sqrt{3}$ structure, and thus the cVBS transition should survive at finite temperatures. In this section, we will further investigate the finite-temperature VBS transitions of the SU(6) Hubbard model.

The finite-size scalings of the VBS order parameters $|D_K|$ at fixed temperatures with $\beta = 10$ and 17 presented in Figs. 2(a) and 2(b), respectively, where $\beta = t/T$. At $\beta = 10$, the system first undergoes a transition from the disordered phase to the VBS phase and reenters the disordered phase, as Hubbard U increases. As shown in the analysis below, based on the calculation of W, the nature of the thermal VBS phase is the same as that in the ground state—the cVBS [16]. The first transition located at $U/t \approx 11.5$ is a finite-temperature version of the ground state Dirac semimetal-to-cVBS transition, while the second transition located around $U/t \approx 13.5$ is the thermal melting of the cVBS state in the Mott-insulating background. At a lower temperature with $\beta = 17$, the VBS order strengths are still nonmonotonic with U, and this feature persists into the ground state as shown in the previous zero-temperature projector DQMC simulations [16]. The reason is that the reduction of the bond kinetic energy scale with increasing U suppresses the strength of VBS ordering. In Figs. 2(c) and 2(d), the finite-size scalings of cVBS order parameters $|D_K|$ are shown for fixed values of U. As temperature decreases, the VBS order develops. At $U/t = 12$, the critical temperature T_c of the cVBS transition is located in the range of $8 < \beta_c < 10$, or, $1/8 > T_c/t > 1/10$. Similarly, at $U/t = 14$, $11 < \beta_c < 12$.

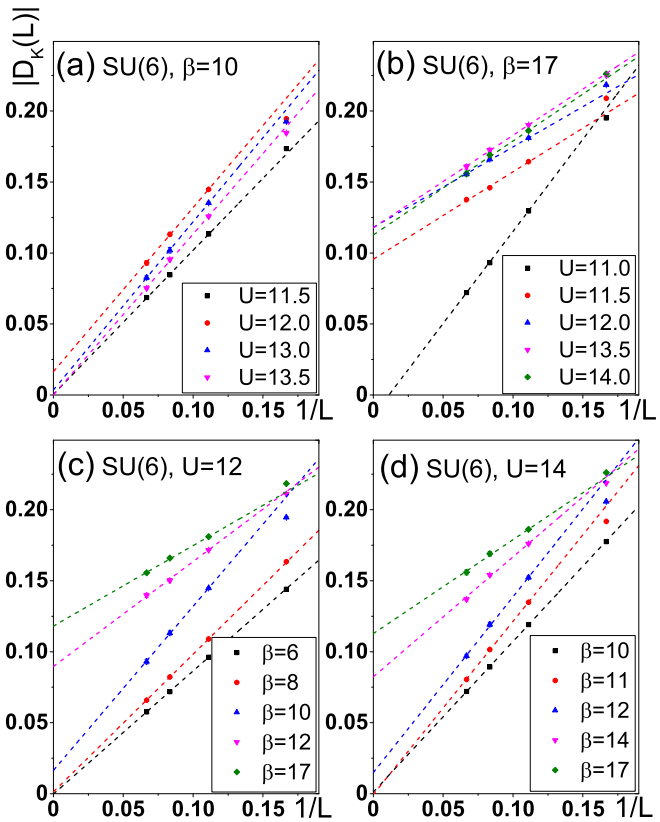

FIG. 2. Finite-size scalings of the VBS dimer parameter $|D_K|$ for the half-filled SU(6) Hubbard model at different values of U and β close to the phase boundary: (a) $\beta = 10$ with different values of U; (b) $\beta = 17$ with different values of U; (c) $U = 12$ with different β; (d) $U = 14$ with different β. The linear fitting is used starting from $L = 9$, and error bars are smaller than data points.

In order to determine the type of the VBS state, we present the finite-size scaling of W for $U/t = 12$ in Fig. 3. At $\beta < 10$, W approaches zero in the thermodynamic limit, which signifies an isotropic disordered phase. At $\beta > 12$, W has already developed a positive value in the thermodynamic limit, which indicates a cVBS ordered phase. The cVBS transition temperature T_c based on the scaling of W is in agreement with that based on the scaling of the VBS dimer parameter.

Based on the above analysis, the finite-temperature phase diagram of the SU(6) honeycomb-lattice Hubbard model is plotted in Fig. 4. The transition temperature T_c increases with U in the interaction range $11 < U/t < 12$, while it decreases as U further increases. The nonmonotonic dependence of T_c on U is consistent with the behavior of the cVBS ordering strength in the ground state, which first increases until reaching the maximum and then decreases as U further increases. The phase diagram Fig. 4 suggests that an SU(6) symmetric Mott insulator with the long-range cVBS order can be formed with an atomic Fermi gas of ^{173}Yb with the hyperfine spin $I = 5/2$, if the ultracold fermions on an optical honeycomb lattice are

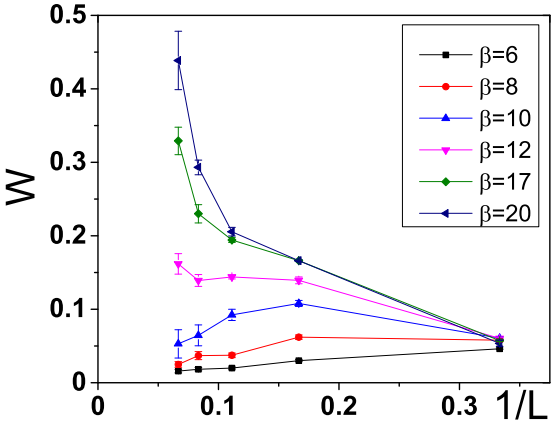

FIG. 3. Finite-size scalings of $W(L)$ for the half-filled SU(6) Hubbard model at $U/t = 12$ with different values of the inverse temperature β.

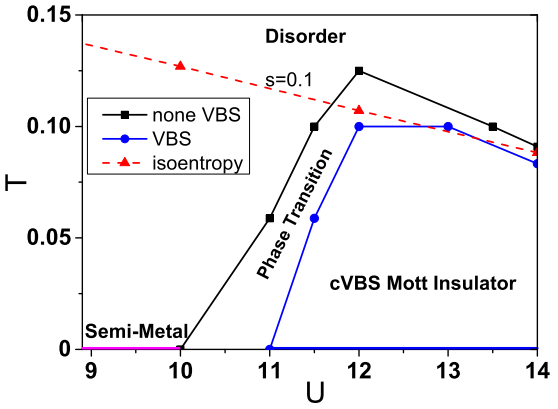

FIG. 4. The finite-temperature phase diagram of the half-filled SU(6) Hubbard model on a honeycomb lattice. The black and the blue lines represent the upper and lower boundaries of the transition temperatures determined by the DQMC simulations. The zero-temperature results are extracted from Ref. [16]. With denser U and T, the two boundaries should merge into one. The red dashed line represents the isoentropy curve of $S_{SU(6)} = 0.1$.

cooled down to the temperature regime below $T/t = 0.1$. Simulations performed in the next section show that this temperature can be achieved by adiabatically increasing the interaction U along the isoentropy curve of $s/k_B \approx 0.1$.

IV. THE POMERANCHUK EFFECT

In this section, we demonstrate, by means of the DQMC simulation, the pronounced Pomeranchuk effect in the half-filled SU(4) and SU(6) Hubbard models on a honeycomb lattice.

A. The entropy-temperature relations

In ultracold atom experiments, entropy, rather than temperature, is a directly measurable physical quantity [23]. We present below the entropy-temperature relations in the half-filled SU(4) and SU(6) Hubbard models on a honeycomb lattice. The entropy per particle can be calculated by:

$$\frac{S(T)}{k_B} = \frac{S(\infty)}{k_B} + \frac{E(T)}{T} - \int_T^\infty dT' \frac{E(T')}{T'^2}, \tag{5}$$

where $E(T)$ is the internal energy per particle at temperature T. In the high temperature limit, there are 2^{2N} possible states on each site and thus $S(\infty) = k_B \frac{\ln 2^{2N}}{N} = k_B \ln 4$ at half filling.

In Fig. 5, we present the entropy per particle of the SU(4) and SU(6) Hubbard models as a function of T at various values of U. In both cases, the $S(T)$ curves cross at a narrow region around a characteristic point (T^*, S^*). The characteristic specific entropy S^* increases with the number of fermion components $2N$ as shown in Table I summarized from the QMC results of this paper and previous publications. (On the square lattice, the Pomeranchuk effect is absent for the SU(2) fermions, because strong AF correlations of SU(2) fermions reduce the entropy capacity, while the multicomponents of a large spin suppress the AF correlations.) Additionally S^* is insensitive to the lattice structure and the associated band structure of SU($2N$) fermions. In fact, S^* denotes the specific

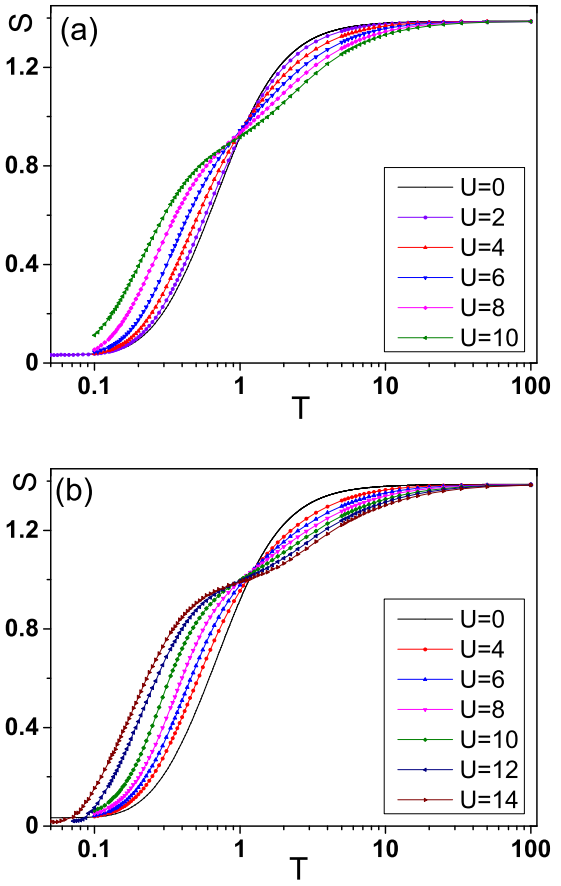

FIG. 5. The entropy per particle as a function of T at different values of U in (a) SU(4) and (b) SU(6) Hubbard models. Note that the $S - T$ curve for $U = 0$ is calculated in Appendix A. The lattice size is $L = 9$.

entropy of each particle coming from the spin channel, which can be estimated as

$$S^* \approx \frac{1}{N} \ln \frac{(2N)!}{N!N!}. \tag{6}$$

In the SU(2), SU(4), and SU(6) cases, S^*'s are approximately $\ln 2 \approx 0.69$, $\frac{1}{2}\ln 6 \approx 0.89$, and $\frac{1}{3}\ln 20 \approx 1.0$, respectively, which excellently agrees with Table I.

We first consider the low specific entropy regime $S < S^*$ in which the entropy per particle increases monotonically with U at a fixed temperature. At weak coupling U, the system is typically in the semimetal state. Its entropy is mainly contributed by fermions near the Dirac points, and

TABLE I. The characteristic specific entropy S^* for spin components $2N = 2,4,6$ with different lattice types.

Symmetry	Lattice type	S^*
SU(2)	Square	N/A [24]
	Honeycomb	~0.65 [25]
SU(4)	Square	~0.9 [26]
	Honeycomb	~0.9
SU(6)	Square	~1.0 [26]
	Honeycomb	~1.0

thus is small due to the vanishing of density of states. As U increases, the system becomes a Mott insulator, and the on-site particle number fluctuations are still frozen in this temperature regime. As a result, fermions on each site contribute to the entropy by means of spin fluctuations. Hence, the semimetal liquidlike phase is more ordered than the solidlike state at the same temperature in the low temperature regime. This is an example of the Pomeranchuk effect, which is first proposed in the ^{3}He system, where increasing pressure can further cool the system in the low temperature regime. The characteristic specific entropy S^* indicates the largest specific entropy for exhibiting the Pomeranchuk effect, above which this effect disappears. The Pomeranchuk effect was found more prominent in the SU($2N$) case due to the enhanced entropy contribution from the spin channel [26–30]. On the honeycomb lattice, the density of states at weak U is further suppressed in the semimetal phase, and the AF correlations are also weakened by the small coordination number. As a result, the Pomeranchuk effect is more prominent than that in the square lattice.

As shown in Fig. 5, the fermion system can be driven to lower temperatures by increasing the Hubbard U adiabatically. Particularly interesting, the isoentropy curve of $S/k_B = 0.1$ intersects the phase boundary near $(U/t = 13, T/t = 0.1)$ as shown in Fig. 4, which suggests a possible scenario for the experimental realization of an SU(6) Mott insulator with the cVBS order. In ultracold atom experiments, the interaction-induced cooling has been achieved in optical lattices by fine tuning the Hubbard U via Feshbach resonances [23].

In the high specific entropy regime $S > S^*$, the entropy from the spin channel has been fully used up. Nevertheless, the contribution from the charge channel, i.e., the fluctuations of the onsite particle number, becomes significant. Increasing U leads to the localization of fermions and thus suppresses charge fluctuations. As a result, the entropy per particle decreases with increasing U at a fixed temperature in this specific entropy regime.

The temperature regime for exhibiting the Pomeranchuk effect also has a lower boundary. On the honeycomb lattice, as shown in Fig. 5, the Pomeranchuk effect becomes pronounced roughly starting at $T/t \sim 0.1$ which is at the same temperature scale of the cVBS ordering. Below this temperature, the cVBS order develops, which dramatically decreases the entropy and then suppresses the Pomeranchuk effect.

It is interesting to note that, similar to the narrow crossing of entropy curves revealed in our simulation, the narrow crossing of specific heat curves was studied by Vollhardt in spin-1/2 correlated systems [31]. Following the same reasoning, in the next section we shall explain analytically the narrowness of the crossing region of entropy curves in the SU($2N$) case.

B. The narrow crossing of entropy curves

Along the same line as Vollhardt's work for the SU(2) case [31], in the SU($2N$) case the conjugate intensive variable associated with U is

$$D(T,U) = \frac{1}{2L^2}\frac{\partial F(T,U)}{\partial U} = \frac{1}{4L^2}\sum_{i\in A\oplus B}(n_i - \langle n_i\rangle)^2, \quad (7)$$

where $F(T,U)$ is the free energy. At half filling, the average particle number per site is $\langle n_i\rangle = N$, and D serves as the variance characterizing the on-site particle number fluctuation. Especially for the SU(2) case, D is just the on-site double occupancy [31–33]. The temperature dependence of D is calculated for a range of Hubbard U, as shown in Fig. 6. It is seen that the on-site particle number fluctuations D are suppressed with increasing U. The temperature dependence of D is nonmonotonic due to the Pomeranchuk effect. For each U, the on-site particle number fluctuation D achieves the minimum at around $T^* \sim t$.

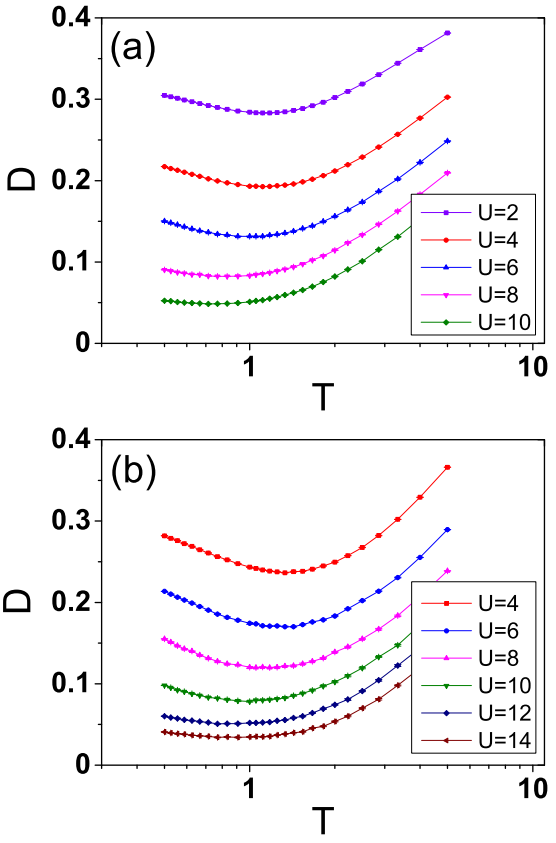

FIG. 6. D as a function of temperature T for (a) SU(4) and (b) SU(6) Hubbard models at half filling. The system size is $L = 9$. Error bars are smaller than the data points.

The entropy per site S and the on-site particle number fluctuation D satisfy the Maxwell relation

$$\frac{\partial S(T,U)}{\partial U} = -\frac{\partial D(T,U)}{\partial T}. \quad (8)$$

We first illuminate why the entropy curves cross. Note that the on-site particle number fluctuations D reach their minima at around $T^* \sim t$ regardless of the coupling strength U, i.e., $\partial D(T^*,U)/\partial T^* = 0$. Using the Maxwell relation (8), one finds that $\partial S(T^*,U)/\partial U = 0$, which implies the crossing of entropy curves at around $T^* \sim t$.

We now explain the narrowness of the crossing region. We expand $S(T^*,U)$ as a power series in $U - U_0$, with U_0 chosen at convenience. To the leading term, one obtains

$$S(T^*,U) \approx S(T^*,U_0)\left[1 + \frac{1}{2}\frac{(U-U_0)^2}{S(T^*,U_0)}\frac{\partial^2 S(T^*,U)}{\partial U^2}\Big|_{U=U_0}\right]. \quad (9)$$

The width of the crossing region is then determined by the curvature of the entropy $S(T,U)$ at T^*. Using Eq. (8) and $\partial D(T^*,U)/\partial T^* = 0$, one obtains

$$\frac{\partial^2 S(T^*,U)}{\partial U^2} = -\frac{\partial}{\partial U}\left[\frac{\partial D(T^*,U)}{\partial T^*}\right] = 0, \tag{10}$$

which guarantees the entropy curves cross at a narrow region around a characteristic point (T^*,S^*).

C. The probability distributions of on-site occupation number

In the SU(2) Hubbard model, the double occupancy is a physical observable in cold atom experiments [33,34]. This quantity behaves slightly nonmonotonic with temperature [32]. In the high temperature regime where thermal fluctuations dominate, the double occupancy can be used as thermometers [35]. In this part, we will simulate the half-filled SU(4) Hubbard model, illustrating the relation between entropy and the distributions of on-site particle numbers.

The probability distribution $P(n)$ of the on-site occupation number n is defined as [26]

$$\begin{aligned} P(0) &= \prod_{\alpha=1}^{4}\left(1-n_i^\alpha\right), \\ P(1) &= \sum_{\alpha=1}^{4} n_i^\alpha \prod_{\beta\neq\alpha}\left(1-n_i^\beta\right), \\ P(2) &= \sum_{\alpha\neq\beta} n_i^\alpha n_i^\beta \prod_{\gamma\neq\alpha\beta}\left(1-n_i^\gamma\right), \end{aligned} \tag{11}$$

where n_i^α is the particle number operator on site i with spin α. The total probability is normalized to unity. The particle number fluctuations also obey the particle-hole symmetry at half filling and thus $P(0) = P(4)$ and $P(1) = P(3)$. In the high temperature limit, the on-site occupation number obeys the binomial distribution, which is $\lim_{T\to\infty} P(k) = C_4^k/2^4$.

In Fig. 7, the relationships between $P(n)$ with $n = 0,1,2$ and the entropy S are presented. The distributions are dramatically nonmonotonic with entropy even in the weak coupling regime, e.g., $U/t = 2,4$, and 6. As expected, at half filling, the most probable distribution of the SU(4) Dirac fermions on each site is the double occupancy, and the deviation from the double occupancy is due to charge fluctuations. These curves show that roughly when $S < S^* \approx 0.89$, the onsite charge fluctuations decrease with increasing entropy, and fermions tend to localize consistent with the Pomeranchuk effect. This seeming discrepancy is due to the dominant entropy contribution from the spin channel. In cold atom experiments, the site-resolved quantum gas microscopy can be used to detect the on-site particle number distributions [36].

V. THE DENSITY AND SPIN RESPONSES

In this section, we investigate the density compressibility and the uniform spin susceptibilities of the half-filled SU($2N$) Hubbard model on a honeycomb lattice.

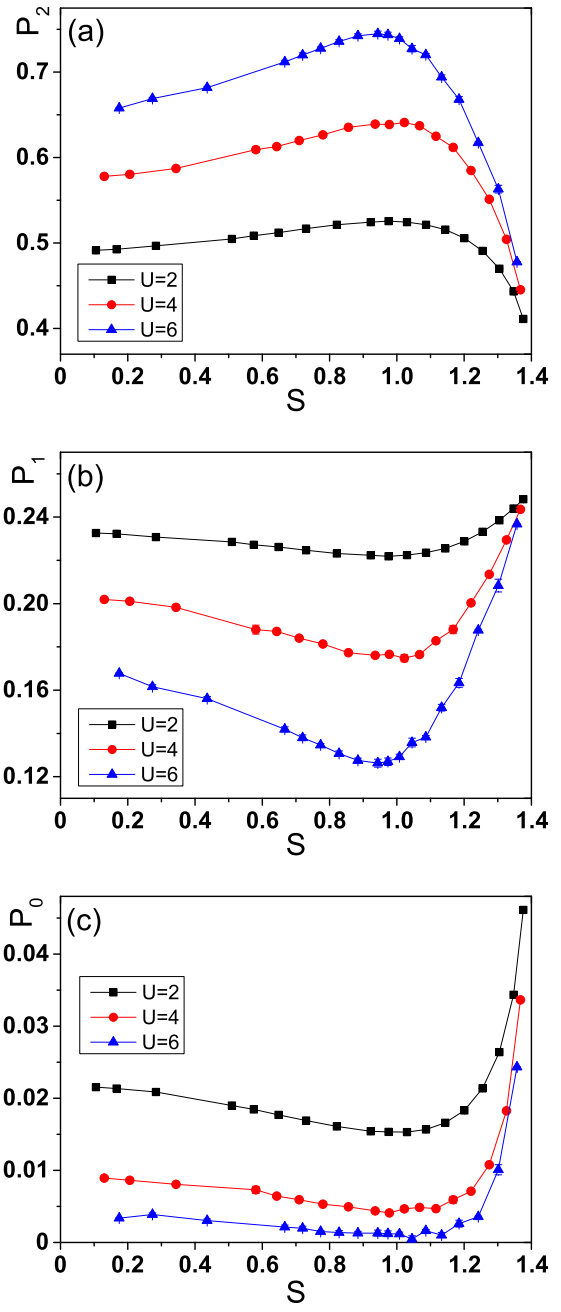

FIG. 7. The probability distributions $P(n)$ of the on-site particle numbers (a) $P(2)$, (b) $P(1)$, and (c) $P(0)$ versus entropy S at different values of U in the half-filled SU(4) Hubbard model. The lattice size is $L = 9$. The lines serve as a guide to the eye, and error bars are smaller than the data points.

A. The density compressibility

The density compressibility is defined as

$$\kappa = \frac{\beta}{2L^2}\left(\left\langle\left(\sum_i n_i\right)^2\right\rangle - \left\langle\sum_i n_i\right\rangle^2\right), \tag{12}$$

which is related to the global density fluctuations. It is an observable in cold atom experiments. The vanishing of κ at low

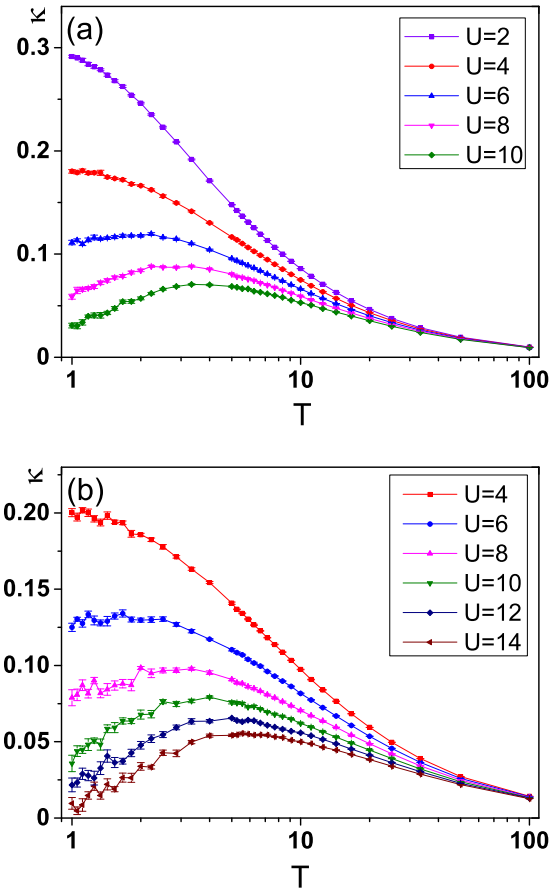

FIG. 8. The density compressibility κ versus T at various values of U in the half-filled (a) SU(4) and (b) SU(6) Hubbard models. The lattice size is $L = 9$.

temperatures is a characteristic signature of the Mott insulating states [37,38].

We present the DQMC simulation results for the density compressibility of SU(4) and SU(6) Hubbard models on a honeycomb lattice in Figs. 8(a) and 8(b), respectively. Here we only calculate κ in the temperature regime corresponding to the $S > S^*$ segment of the $S(T)$ curves. At low temperatures, the simulation of κ becomes numerically unstable as explained in Appendix B. At very high temperatures $T \gg U$, $\kappa(T)$ behaves like that of a classic ideal gas, i.e., $\kappa \sim 1/T$, which means charge incoherence. On the other hand, increasing U while fixing T suppresses the compressibility. However, in the zero temperature limit not shown in Fig. 8, κ should go to zero both in the Dirac semimetal phase due to the vanishing of density of states and in the cVBS state due to the charge gap opening. Consequently, the $1/T$ divergence of κ stops when T decreases to a certain temperature scale dependent of t and U. At large values of $U > U_c$ where U_c is the critical interaction strength for the emergence of the cVBS ground state, κ becomes decreasing along with lowering T after reaching the maximal value at a temperature comparable to U ($U_c \approx 7$ and 11 in the SU(4) and SU(6) cases, respectively [16]).

Note that, in the SU(6) case with $U/t = 14$, κ is nearly suppressed to zero at $T/t \sim 1$, a temperature scale comparable to the bandwidth but still much smaller than the Hubbard interaction. This is also the temperature scale for the thermal melting of the cVBS state as shown in Fig. 4. Thus the finite-temperature disordered states outside the cVBS phase exhibit different characters: In the weak coupling side, it is a finite-temperature semimetal state, while in the strong coupling side, it is a finite-temperature Mott-insulating state with thermally melted cVBS order. Nevertheless, they can be smoothly connected at finite temperatures.

B. The uniform spin susceptibilities

The uniform spin susceptibility χ is defined as

$$\chi = \frac{\beta}{2L^2} \sum_{i,j} S_{\text{spin}}(i,j), \tag{13}$$

where $S_{\text{spin}}(i,j)$ is the SU($2N$) version of the equal-time spin-spin correlation:

$$S_{\text{spin}}(i,j) = \frac{1}{(2N)^2 - 1} \sum_{\alpha,\beta} \langle S_{\alpha\beta,i} S_{\beta\alpha,j} \rangle. \tag{14}$$

Note that $S_{\alpha\beta,i} = c^\dagger_{\alpha,i} c_{\beta,i} - \frac{\delta^{\alpha\beta}}{2N} \sum_{\gamma=1}^{2N} c^\dagger_{\gamma,i} c_{\gamma,i}$ are the generators of an SU($2N$) group and satisfy the commutation relation $[S_{\alpha\beta}, S_{\gamma\delta}] = \delta^{\beta\gamma} S_{\alpha\delta} - \delta^{\alpha\delta} S_{\gamma\beta}$.

In Fig. 9, the uniform spin susceptibility $\chi(T)$'s of the SU(4) and SU(6) Hubbard models on a honeycomb lattice are plotted for various values of Hubbard U. The high temperature behaviors of $\chi(T) \sim 1/T$ obey the Curie-Weiss law, which shows the spin incoherence. Again this divergence is suppressed at low temperatures since in the zero temperature limit, $\chi(T)$ approaches zero in both the Dirac semimetal phase and the cVBS phase. In the former case, it is because of the vanishing of density of states, while in the latter case, it is due to the cVBS phase being a spin gapped phase. Thus a peak in each $\chi(T)$ curve must develop in the full range of the Hubbard U. In the strong coupling regime, the peak is located around the super-exchange energy scale $J \approx 4t^2/U$. In contrast, the peak location in the weak coupling regime is mostly determined by the bandwidth t, and consequently the peak is located at the energy scale in which the density of states becomes linear.

One observation from Fig. 9 is that $\chi(T)$ increases monotonically with U at a fixed temperature. In the weak coupling regime, this is consistent with the mean-field analysis concluding that the uniform spin susceptibility χ is enhanced by the repulsive interaction [39]. In the strong coupling regime, increasing U enhances the amplitudes of the onsite spin moments by suppressing the charge fluctuations, and thus $\chi(T)$ is also increased. At small values of U, a tiny upturn occurs in the $\chi(T)$ curve at low temperatures, which is caused by the finite-size effect [40].

Considering the SU(4) and SU(6) Hubbard models on a honeycomb lattice, the AF ordering does not occur even in the ground state. Nevertheless, we also present the simulation results of the AF structure factors and nearest-neighbor spin-spin correlations in Appendix D.

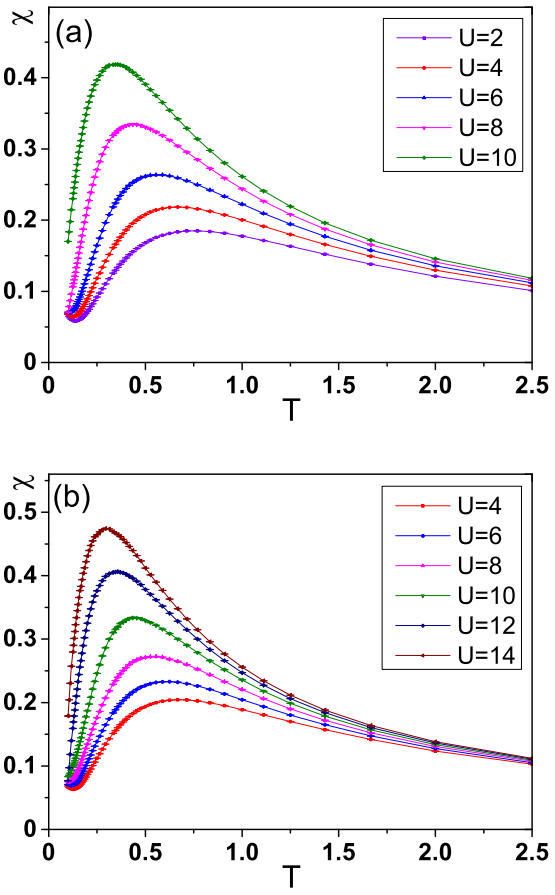

FIG. 9. The uniform spin susceptibilities χ versus temperature T at various values of U in the half-filled (a) SU(4) and (b) SU(6) Hubbard models. The lattice size is $L = 9$. Error bars are smaller than the data points.

VI. CONCLUSIONS

In summary, we have employed the large-scale DQMC simulations to study the effects of SU($2N$) symmetries on thermodynamic properties of Dirac fermions. The Dirac fermions are described in terms of the SU($2N$) Hubbard model on a honeycomb lattice which captures the interplay between charge and spin degrees of freedom. We have simulated the finite-temperature properties of SU(4) and SU(6) cases, including the thermal VBS phase transition, the Pomeranchuk effect, the density compressibility, and spin susceptibilities.

We use the SU(6) case as an example to study the thermal phase transition between the disordered state and the cVBS state on a honeycomb lattice. In the SU(2) honeycomb-lattice Hubbard model, the Mott insulating phase at $T = 0$ exhibits the AF ordering which breaks the continuous SU(2) symmetry and thus cannot exist at finite temperatures. Nevertheless, the cVBS order in the SU(6) case only breaks a discrete symmetry and does occur in the thermal transition. Based on the above reasoning, the thermal cVBS phase transition is also expected in the simulations of the SU(4) honeycomb-lattice Hubbard model, though the cVBS order is weaker compared with the SU(6) case. The simulation of entropy-temperature relations shows that the $S(T)$ curves with different Hubbard U cross at a narrow region around a characteristic point (T^*, S^*) characterizing the onset of the Pomeranchuk effect. This characteristic specific entropy S^* comes from the local spin moment contribution estimated as $S^* \approx \frac{1}{N} \ln \frac{(2N)!}{N!N!}$. As demonstrated in our DQMC simulations, the SU(6) cVBS Mott insulating state can be reached along the isoentropy curve $S/k_B = 0.1$ by the interaction-induced adiabatic cooling, which sheds light on future explorations of novel states of matter with ultracold ^{173}Yb experiments.

It is worth noting that a plateau of $S = S^*$ is expected to appear in a single $S(T)$ curve when Hubbard U is large enough, due to the full release of spin entropy. In fact, the roles of spin and charge channels in entropy production are separated at around $S = S^*$, when the Coulomb repulsion U becomes stronger than the critical interaction that leads to the emergence of the cVBS ground state. Interestingly, in the weak and intermediate coupling regimes, the simulated $S(T)$ curves cross at around a characteristic point where $S = S^*$, though S^* is not noticeable in a single $S(T)$ curve. The underlying physics of this special phenomenon may be revealed in future studies.

ACKNOWLEDGMENTS

Z.Z. and Y.W. gratefully acknowledge financial support from the National Natural Science Foundation of China under Grants No. 11574238 and No. 11328403. D.W. acknowledges the support from National Natural Science Foundation of China (11504164). C.W. is supported by the NSF DMR-1410375 and AFOSR FA9550-14-1-0168. C.W. acknowledges the support from the Presidents Research Catalyst Awards of University of California. This work made use of the facilities of Tianhe-2 at the China's National Supercomputing Centre in Guangzhou.

APPENDIX A: THE FINITE-SIZE EFFECT ON ENTROPY

In the weak coupling regime, the finite-size effect is significant at low temperatures. We investigate the finite-size dependence of entropy per particle of a half-filled SU($2N$) tight-binding model on a honeycomb lattice. The entropy per particle can be calculated by [41]:

$$S(T, U = 0) = -\frac{1}{L^2} \sum_k (f \ln f + (1 - f) \ln(1 - f)), \tag{A1}$$

where f is the Fermi-Dirac distribution. As shown in Fig. 10(a), the residue entropy caused by finite-size effect decreases with increasing lattice size. It is seen that the finite-size effect is not severe for $L = 9$ with $S/k_B \geqslant 0.1$.

We can see in Fig. 10(b) that the finite-size effect still exists for $U = 6$ in the semimetal region. But the dimer formation in a bond lifts degeneracy and thus lowers the entropy in the strong coupling regime, as shown in Fig. 10(c) where $U = 12$. Moreover, the cVBS correlation length is much larger than the lattice size. As a result, the finite-size effect is weak in the cVBS region. Hence the isoentropy curve demonstrating Pomeranchuk cooling in Fig. 4 is a reasonable estimate in the thermodynamic limit.

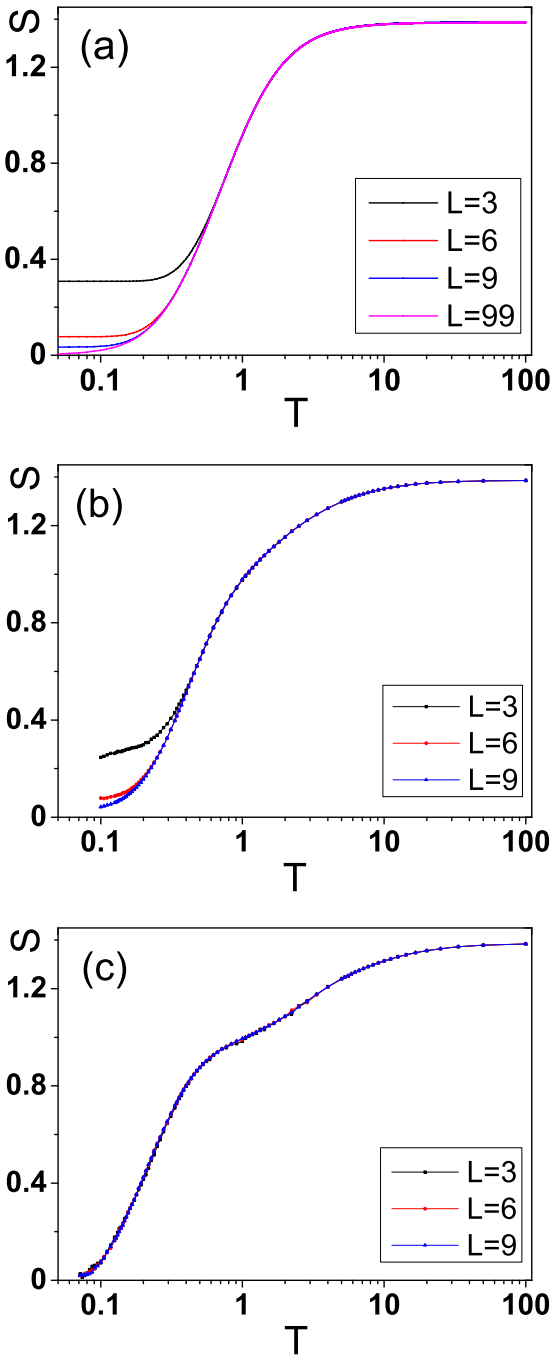

FIG. 10. The finite-size dependence of entropy per particle of the half-filled SU(6) Hubbard model with parameters (a) $U = 0$, (b) $U = 6$, and (c) $U = 12$.

APPENDIX B: IMAGINARY PART OF THE COMPRESSIBILITY

In our simulations, the Hubbard-Stratonovich transformation is performed in the density channel as below,

$$e^{\frac{\Delta\tau U}{2}(n_j-N)^2} = \frac{1}{4}\sum_{l=\pm1}\gamma_j(l)e^{i\eta_j(l)(n_j-N)}, \tag{B1}$$

where γ and η are two sets of parameters. According to Ref. [22], in the cases of $2N = 2,4$, and 6, the Ising fields

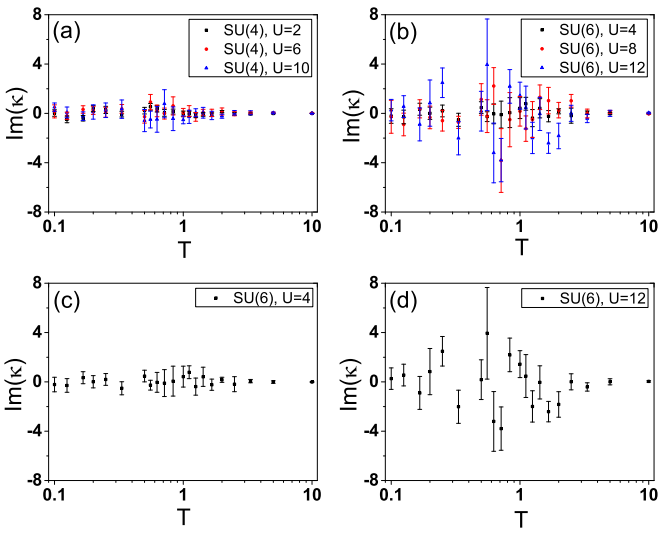

FIG. 11. The imaginary part of compressibility $\mathrm{Im}(\kappa)$ versus T with different U and $2N$: (a) SU(4) case with different U; (b) SU(6) case with different U; (c) SU(6) case with $U = 4$; (d) SU(6) case with $U = 12$.

can take values of

$$\gamma(\pm1) = \frac{-a(3+a^2)+d}{d},$$

$$\gamma(\pm2) = \frac{a(3+a^2)+d}{d},$$

$$\eta(\pm1) = \pm\cos^{-1}\left\{\frac{a+2a^3+a^5+(a^2-1)d}{4}\right\},$$

$$\eta(\pm2) = \pm\cos^{-1}\left\{\frac{a+2a^3+a^5-(a^2-1)d}{4}\right\},$$

where $a = e^{-\Delta\tau U/2}$, and $d = \sqrt{8+a^2(3+a^2)^2}$.

Because the diagonal term is complex, the decomposed fermion bilinear operators are no longer Hermitian. If all the configurations are reached when performing the path integrals, the Hermitian of the many-body Hamiltonian is recovered. However, since the importance sampling is used in the Monte Carlo integrations, the imaginary part of a physical quantity is only statistically zero.

The compressibility $\kappa(T)$ is related to the global density-density correlations rather than local on-site correlations. In Fig. 11, we calculate the imaginary part of $\kappa(T)$ with different values of T, U, and $2N$. $\mathrm{Im}(\kappa)$ fluctuates around zero severely in the low temperature regime. Furthermore, it is seen that fluctuations turn to be increasingly severe when increasing the value of $2N$ [see Figs. 11(a) and 11(b)] or the Hubbard U [see Figs. 11(c) and 11(d)].

APPENDIX C: THE BEHAVIOR OF AVERAGE SIGN IN THE MOTT REGION

The chemical potential is set to zero (at half filling) in our DQMC simulations, which ensures the sign problem is absent. We also test the average sign in the Mott region of the SU(6) Hubbard model when the chemical potential μ deviates

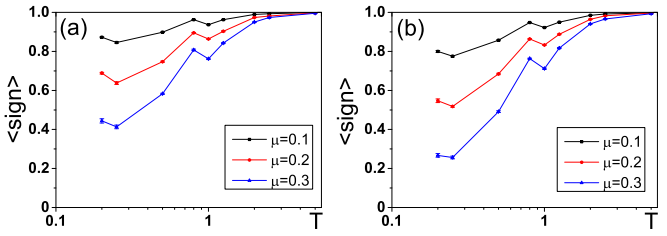

FIG. 12. The average sign as a function of T for various chemical potentials at (a) $U = 12$ and (b) $U = 14$ in the SU(6) Hubbard model on a honeycomb lattice with $L = 9$. Error bars are smaller than the data points.

from zero (away from half filling). In this case, an extra term $H_\mu = -\mu \sum_i n_i$ is added to the original Hamiltonian, Eq. (1). As shown in Fig. 12, the average signs deviate quickly from unity as the temperature decreases and the sign problem becomes severe when temperatures are lower than $T \sim t$, a temperature scale set by the numerical instability test in Appendix B.

APPENDIX D: THE AF STRUCTURE FACTORS AND NEAREST-NEIGHBOR SPIN-SPIN CORRELATIONS

The AF structure factors are defined as

$$S_{AF} = \frac{1}{2L^2} \sum_{i,j} (-1)^{i+j} S_{\text{spin}}(i,j). \tag{D1}$$

As shown in Fig. 13, we simulate the AF structure factor S_{AF} of the SU(4) and SU(6) Hubbard models on a $2 \times 9 \times 9$ honeycomb lattice. With decreasing temperatures, the S_{AF}'s of the SU($2N$) ($N = 2,3$) Dirac fermions increase slowly and saturate eventually when $2 \leqslant U/t \leqslant 6$, while they increase rapidly when $8 \leqslant U/t \leqslant 10$.

In Fig. 14, the β dependence of the SU(6) AF structure factor S_{AF} with $U/t = 14$ are shown for different lattice sizes from $L = 3$ to $L = 15$. S_{AF} increases monotonically with inverse temperature β. But S_{AF} is size independent even at low temperatures $T/t \sim 1/10$, which indicates that the AF

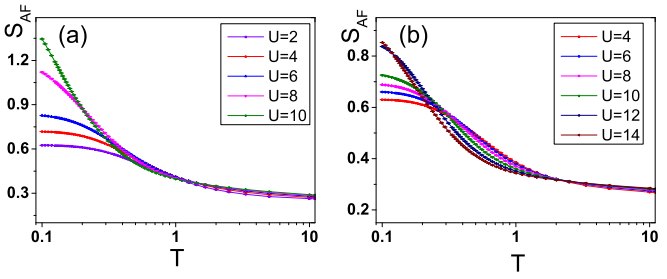

FIG. 13. The AF structure factors S_{AF} versus temperature T at various values of U in the half-filled (a) SU(4) and (b) SU(6) Hubbard models. The lattice size is $L = 9$. Error bars are smaller than the data points.

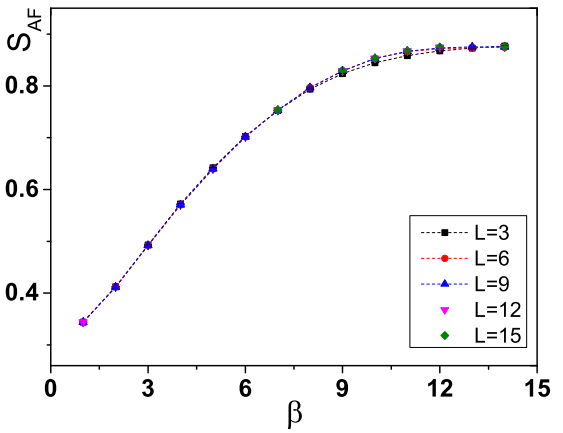

FIG. 14. The AF structure factor S_{AF} of the SU(6) Hubbard model with $U = 14$ is plotted as a function of β for different lattice sizes L. The dashed lines serve as a guide to the eye, and error bars are smaller than the data points.

correlation length is smaller than lattice size $L = 3$. This is another evidence that the long-range AF order is absent in the half-filled SU(6) Hubbard model on a honeycomb lattice.

The nearest-neighbor spin-spin correlations are defined as

$$S_{nn} = \frac{1}{zL^2} \sum_{i \in A, \vec{e}_j} S_{\text{spin}}(i, i + \vec{e}_j), \tag{D2}$$

where z is the coordination number. In Fig. 15, we present the nearest-neighbor spin-spin correlations S_{nn} in the half-filled SU(4) and SU(6) Hubbard models. At high temperatures $T/t \sim 10$, $|S_{nn}|$ is independent of the Hubbard U, which shows spin incoherence. In contrast, at low temperatures $T/t \sim 0.1$, increasing U enhances the nearest-neighbor AF correlations, and thus $|S_{nn}|$ increases.

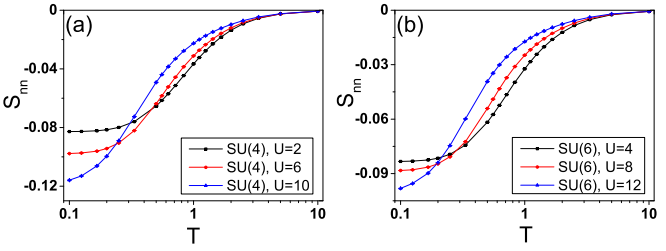

FIG. 15. The nearest-neighbor spin-spin correlation S_{nn} versus temperature T at various values of U in the half-filled (a) SU(4) and (b) SU(6) Hubbard models. The lattice size is $L = 9$. Error bars are smaller than the data points.

[1] A. H. Castro Neto, F. Guinea, N. M. R. Peres, K. S. Novoselov, and A. K. Geim, Rev. Mod. Phys. **81**, 109 (2009).

[2] T. Paiva, R. T. Scalettar, W. Zheng, R. R. P. Singh, and J. Oitmaa, Phys. Rev. B **72**, 085123 (2005).

[3] Z. Y. Meng, T. C. Lang, S. Wessel, F. F. Assaad, and A. Muramatsu, Nature (London) **464**, 847 (2010).

[4] F. F. Assaad and I. F. Herbut, Phys. Rev. X **3**, 031010 (2013).

[5] F. Parisen Toldin, M. Hohenadler, F. F. Assaad, and I. F. Herbut, Phys. Rev. B **91**, 165108 (2015).

[6] Y. Otsuka, S. Yunoki, and S. Sorella, Phys. Rev. X **6**, 011029 (2016).

[7] C. Wu, J. P. Hu, and S. C. Zhang, Phys. Rev. Lett. **91**, 186402 (2003).

[8] C. Wu, Mod. Phys. Lett. B **20**, 1707 (2006).

[9] A. V. Gorshkov, M. Hermele, V. Gurarie, C. Xu, P. S. Julienne, J. Ye, P. Zoller, E. Demler, M. D. Lukin, and A. M. Rey, Nat. Phys. **6**, 289 (2010).

[10] C. Wu, Nat. Phys. **8**, 784 (2012).

[11] S. Taie, Y. Takasu, S. Sugawa, R. Yamazaki, T. Tsujimoto, R. Murakami, and Y. Takahashi, Phys. Rev. Lett. **105**, 190401 (2010).

[12] B. J. DeSalvo, M. Yan, P. G. Mickelson, Y. N. Martinez de Escobar, and T. C. Killian, Phys. Rev. Lett. **105**, 030402 (2010).

[13] S. Taie, R. Yamazaki, S. Sugawa, and Y. Takahashi, Nat. Phys. **8**, 825 (2012).

[14] G. Pagano, M. Mancini, G. Cappellini, P. Lombardi, F. Schäfer, H. Hu, X.-J. Liu, J. Catani, C. Sias, M. Inguscio, and L. Fallani, Nat. Phys. **10**, 198 (2014).

[15] C. Hofrichter, L. Riegger, F. Scazza, M. Höfer, D. R. Fernandes, I. Bloch, and S. Fölling, Phys. Rev. X **6**, 021030 (2016).

[16] Z. Zhou, D. Wang, Z. Y. Meng, Y. Wang, and C. Wu, Phys. Rev. B **93**, 245157 (2016).

[17] B. Roy, V. Juričić, and I. F. Herbut, Phys. Rev. B **87**, 041401 (2013).

[18] Z.-X. Li, Y.-F. Jiang, S.-K. Jian, and H. Yao, arXiv:1512.07908.

[19] M. M. Scherer and I. F. Herbut, Phys. Rev. B **94**, 205136 (2016).

[20] S.-K. Jian and H. Yao, arXiv:1610.07603.

[21] R. Blankenbecler, D. J. Scalapino, and R. L. Sugar, Phys. Rev. D **24**, 2278 (1981).

[22] D. Wang, Y. Li, Z. Cai, Z. Zhou, Y. Wang, and C. Wu, Phys. Rev. Lett. **112**, 156403 (2014).

[23] I. Bloch, J. Dalibard, and W. Zwerger, Rev. Mod. Phys. **80**, 885 (2008).

[24] T. Paiva, R. Scalettar, M. Randeria, and N. Trivedi, Phys. Rev. Lett. **104**, 066406 (2010).

[25] B. Tang, T. Paiva, E. Khatami, and M. Rigol, Phys. Rev. B **88**, 125127 (2013).

[26] Z. Zhou, Z. Cai, C. Wu, and Y. Wang, Phys. Rev. B **90**, 235139 (2014).

[27] K. R. A. Hazzard, V. Gurarie, M. Hermele, and A. M. Rey, Phys. Rev. A **85**, 041604 (2012).

[28] Z. Cai, H.-h. Hung, L. Wang, D. Zheng, and C. Wu, Phys. Rev. Lett. **110**, 220401 (2013).

[29] L. Bonnes, K. R. A. Hazzard, S. R. Manmana, A. M. Rey, and S. Wessel, Phys. Rev. Lett. **109**, 205305 (2012).

[30] L. Messio and F. Mila, Phys. Rev. Lett. **109**, 205306 (2012).

[31] D. Vollhardt, Phys. Rev. Lett. **78**, 1307 (1997).

[32] F. Werner, O. Parcollet, A. Georges, and S. R. Hassan, Phys. Rev. Lett. **95**, 056401 (2005).

[33] R. Jördens, N. Strohmaier, K. Günter, H. Moritz, and T. Esslinger, Nature (London) **455**, 204 (2008).

[34] N. Strohmaier, D. Greif, R. Jördens, L. Tarruell, H. Moritz, T. Esslinger, R. Sensarma, D. Pekker, E. Altman, and E. Demler, Phys. Rev. Lett. **104**, 080401 (2010).

[35] R. Jördens, L. Tarruell, D. Greif, T. Uehlinger, N. Strohmaier, H. Moritz, T. Esslinger, L. De Leo, C. Kollath, A. Georges, V. Scarola, L. Pollet, E. Burovski, E. Kozik, and M. Troyer, Phys. Rev. Lett. **104**, 180401 (2010).

[36] P. M. Preiss, R. Ma, M. E. Tai, J. Simon, and M. Greiner, Phys. Rev. A **91**, 041602 (2015).

[37] U. Schneider, L. Hackermüller, S. Will, T. Best, I. Bloch, T. A. Costi, R. W. Helmes, D. Rasch, and A. Rosch, Science **322**, 1520 (2008).

[38] P. M. Duarte, R. A. Hart, T.-L. Yang, X. Liu, T. Paiva, E. Khatami, R. T. Scalettar, N. Trivedi, and R. G. Hulet, Phys. Rev. Lett. **114**, 070403 (2015).

[39] P. Fazekas, *Lecture Notes on Electron correlation and Magnetism* (World Scientific, Singapore, 1999).

[40] At $U = 0$, the spin susceptibilities are calculated by $\chi(T) = -\int_{-\infty}^{\infty} d\epsilon \frac{\partial f}{\partial \epsilon} \rho(\epsilon)$, where f is the Fermi-Dirac distribution and ρ is the density of states. In a finite system, the integration can be transformed into a summation. So the discrete energy levels will take the responsibility for the upturn. In Ref. [42], a small upturn also appeared in $\chi(T)$.

[41] A.-M. Daré, L. Raymond, G. Albinet, and A.-M. S. Tremblay, Phys. Rev. B **76**, 064402 (2007).

[42] N. M. R. Peres, F. Guinea, and A. H. Castro Neto, Phys. Rev. B **73**, 125411 (2006).